MRI geometric distorsion: A simple approach to correcting the effects of non-linear gradient fields

Serge Langlois, Michel Desvignes, Jean-Marc Constans, Marinette Revenu

MRI Geometric Distortion: a simple approach to correcting the effects of non-linear gradient fields

S. Langlois, PhD • M. Desvignes, Assistant Professor •

J.M. Constans, MD • M. Revenu, Professor

Correspondence:

Serge Langlois

GREYC-ISMRA, 6 bd Maréchal Juin, 14050 Caen (France)

Tel: +33 (0)231 45 29 20, Fax: +33 (0)231 45 26 98

Email: Serge.Langlois@greyc.ismra.fr

Abstract

We present a method to correct intensity variations and voxel shifts caused by non-linear gradient fields in Magnetic Resonance Images. The principal sources of distortion are briefly exposed, as well as the methods of correction currently in use. The implication of the gradient fields non-linearities on the signal equations are described in a detailed way for the case of 2D and 3D Fourier imagery. A model of these non-linearities, derived from the geometry of the gradient coils, is proposed and then applied in post-processing to correct any images regardless of the acquisition sequence. Initial position errors, as large as 4 mm (i.e. 4 voxels of 1x1x1.4 mm^3) before correction, are reduced to less than the voxel sizes after correction.

Keywords

Magnetic resonance imaging • Image distortion correction • Non-linear gradient fields

INTRODUCTION

Magnetic Resonance Imaging has entered clinical practice about fifteen years ago, and has become one of the most widely used imaging modalities (i, ii). Its capacity to produce high-resolution images of superior tissue contrast within a few minutes makes it more attractive than other modalities for clinical applications such as stereotactic neurosurgery. More recently, MR Angiography and Functional MRI also gained increasing interest as cerebral imaging tools (iii, iv, v). MRI, however, suffers from important geometric distortions, leading to pixel shifts and intensity variations in the acquired images (vi, vii). Many reports underlined the importance of these

variations, reaching several millimeters in certain areas of the field of view, thus showing the difficulty of precisely locating the anatomic internal structures (viii, ix).

Machine-dependent and patient-dependent effects are both at the origin of the most important distortions. The main effects are the chemical shift, the magnetic susceptibility, eddy currents, B_0 inhomogeneity and gradient non-linearity. Chemical shift arises when a voxel is composed of several tissues with different precession frequencies (e.g., water and fat). With a different response from each tissue to the different RF pulses, this physically unique voxel is imaged in several voxels of the reconstructed volume. Applying a selective saturation before the acquisition in order to extract unwanted tissue from MR signal can minimize chemical shift effects (x). Magnetic susceptibility effects occurs at the interface of tissues with different magnetic susceptibilities (and especially air/tissue interfaces). A local gradient field is created that is superimposed on the main B_0 field, disturbing spatial encoding of the voxels (xi). This effect usually requires a particular treatment that often increases the acquisition time (xii, xiii). Eddy currents are induced in the main structure of the magnet by rapid switching of the current in the gradient coils. A fine calibration and the use of shielded coils usually gets rid of eddy currents and other B_0 offsets (xiv, xv). Gradient fields, that depend on the coils geometry, are usually specific to each MR scanner. Their effect on the accuracy of the reconstructed MR images is the only one considered in this study.

We propose in this article a method to correct gradient field non-linearities for the case of Fourier transform imaging. A theoretical model is first proposed for 2D and 3D imagery. A phantom-based method is then presented to obtain the analytical expressions of three correction functions. Voxel shifts and intensity variations are adjusted in post-processing using the correction functions. The method is validated by comparing

corrected images with theoretical images of the phantom, with images processed with another correction scheme (GRAD WARP) and finally, with a CT scan of the phantom..

Partial List of Symbols

B_0	Static magnetic field
$\omega_0 = \gamma B_0$	Larmor frequency
Fe	Sample bandwidth
M(x)	Sample magnetization at time t = 0. It includes the dependence on the spin density and the acquisition sequence with the flip angle and the *TR/T1* decay
FOV_x, FOV_y, FOV_z	Selected fields of view in the *x, y, z* directions
N_x , N_y , N_z	Number of samples, repetitions, slices
Δx , Δy , Δz	Voxel sizes, given by $\Delta i = \frac{FOV_i}{N_i}$
τ_x , τ_y , τ_z	Duration of the readout, phase encoding and slice selection gradients
$G_l(t)$	Theoretical strength of the readout gradient, given by $\int_0^{\tau_x} G_l(t)\,dt = \frac{2\pi}{\gamma\, FOV_x}$. If constant during the acquisition, it is simplified by $G_l = \frac{2\pi\ Fe}{\gamma\ FOVx}$
$k\ G_c(t)$	Theoretical strength of the phase encoding gradient at the k^{th} repetition, given by $k\int_0^{\tau_y} G_c(t)\,dt = \frac{2\pi}{\gamma\, FOV_y}k$. If

constant, $G_c(t)$ is simplified by $G_c = G_{ref} \frac{FOV_{\max}}{FOV_y}$, where $G_{ref}.FOV_{max}$ is a machine-dependent constant

$p\ G_p(t)$ Theoretical strength of the p^{th} slice selection gradient, given by $p \int_0^{\tau_z} G_p(t)\,dt = \frac{2\pi}{\gamma\, FOV_z}\, p$. If constant, $G_p(t)$ is simplified by $G_p = G_{ref} \frac{FOV_{\max}}{FOV_z}$

THEORY

One dimension : principle of the correction

The acquired MRI signal can be expressed in one dimension as (xvi, xvii)

$$s(t) = \int_{FOVx} M(x) e^{j.\varphi(x,t)} e^{-\frac{t+TE}{T2(x)}} dx \qquad (1)$$

In the ideal case of a homogeneous B_0 field, the phase at time t due to B_0 superimposed on a constant readout gradient is given by

$$\varphi(x,t) = \gamma \int_0^t B_x(x,t')\,dt' = \gamma\left(B_0 + G_{rx}(x)\,t\right) \qquad (2)$$

where $G_{rx}(x)$ is the physically applied (i.e. non-linear) gradient. Signal demodulation leads to the temporal signal

$$S(t) = \int_{FOVx} M(x)\, e^{j\gamma G_{rx}(x)t} e^{-\frac{t+TE}{T2(x)}}\, dx \qquad (3)$$

A Fourier transform of $S(t)$ gives the spatial signal

$$I(x) = \frac{1}{\tau_x} \int_0^{\tau_x} \left[\int_{FOVx} M(x')\, e^{j\gamma G_{rx}(x')t} e^{-\frac{t+TE}{T2(x')}}\, dx' \right] e^{-j\gamma G_x(x)t}\, dt \qquad (4)$$

where $G_x(x)$ is here the theoretical gradient used for the reconstruction, given by $G_x(x) = x\, G_l$.

The real gradient is characterised in our model as the product of the theoretical gradient strength and a function of the position only: $G_{rx}(x) = f(x)\, G_l$.

The expression of the intensity becomes:

$$\begin{aligned} I(x) &= \frac{1}{\tau_x}\int_0^{\tau_x}\left[\int_{FOVx} M(x')\, e^{j\gamma f(x') G_l t} e^{-\frac{t+TE}{T2(x')}}\, dx'\right] e^{-j\gamma x G_l t}\, dt \\ &= \int_{FOVx} M(x')\, e^{-\frac{TE}{T2(x')}}\, H(x - f(x'))\, dx' \end{aligned} \tag{5}$$

where $H(x)$ represents the Fourier transform of the rectangular gradient G_l, given by :

$$H(x) = \frac{\sin(\pi \frac{x}{\Delta x})}{\pi\, x} \tag{6}$$

The variable change $X = f(x')$ in the last expression of the intensity gives :

$$\begin{aligned} I(x) &= \frac{1}{\tau_x}\int_0^{\tau_x}\left[\int_{f^{-1}(FOVx)} M\left(f^{-1}(X)\right)\frac{df^{-1}(X)}{dX} e^{j\gamma X G_l t}\; e^{-\frac{t+TE}{T2\left(f^{-1}(X)\right)}}\, dX\right] e^{-j\gamma x G_l t}\, dt \\ &= M(x) e^{-\frac{TE}{T2(x)}} \otimes H(f(x)) \end{aligned} \tag{7}$$

Using the same convolution notation, the undistorted theoretical image ($X=x'$) is :

$$I_t(x) = M(x) e^{-\frac{TE}{T2(x)}} \otimes H(x) \tag{8}$$

The expression of $I(x)$ shows that the non-linearities act on the position as well as on the intensity of the theoretical signal $I_t(x)$, by changing the shape of the function $H(x)$.

The correction is based on a property of the point spread function H(x), which is invariant with the convolution. This can be expressed by :

$$H(x) \otimes H(x) = H(f(x)) \otimes H(f(x)) = H(x) \tag{9}$$

The relation between the undistorted theoretical image and the acquired image is therefore :

$$I_t(x) = I_t(f(x)) \otimes H(f(x)) \tag{10}$$

A corrected image $I_t(x)$ can be obtained at the point x by the convolution of the acquired image with the function H, both shifted of an amount $f(x)$.

Application to 2D and 3D imagery

As outlined in appendix, non-linear gradient fields act in 2D on the actual magnetization as soon as its creation by the selective RF pulse. However the slice profile can be corrected, knowing the non-linearity function $f_z(x,y,z)$ of the slice encoding direction z, by using the relation between the theoretical magnetization M_t and the received magnetization M_r :

$$M_t(x,y,z) = \frac{\partial f_z(x,y,z)}{\partial z} M_r\left(x,y,f_z(x,y,z)\right) \tag{11}$$

The slice profile can be corrected in 2D imagery by shifting each point of the acquired image by the amount $f_z(x,y,z)$ in the z direction. Intensity misregistration is corrected by the moderation factor $\partial f_z(x,y,z)/\partial z$.

The various steps of the reconstruction process under the action of non-linear gradient fields bring to the relationship between corrected and acquired images I_c and I_a :

$$I_c(x,y,z) = I_a(X,Y,Z)\frac{\partial Z}{\partial z} \otimes H_x(X) \otimes H_y(Y) \tag{12}$$

where $H_x(x)$ and $H_y(y)$ represent respectively the Fourier transforms of the readout and phase encoding gradient profiles, and the variables X, Y and Z are given by the system :

$$\begin{cases} X = f_x(x,y,Z) \\ Y = f_y(x,y,Z) \\ Z = f_z(x,y,z) \end{cases} \tag{13}$$

The functions $f_x(x,y,z)$ and $f_y(x,y,z)$ account for the non-linearity of the readout and phase encoding directions. We notice that in 2D imagery, the correction must be carried out in a given order (X and Y being related to Z), since slice profile variations must be corrected before applying planar shifts.

In 3D imagery the RF pulse, applied in 2D in order to select a specific slice, is now applied so as to select the entire volume at the same time. The relationship between corrected and acquired image is then :

$$I_c(x,y,z) = I_a(X,Y,Z) \otimes H_x(X) \otimes H_y(Y) \otimes H_z(Z) \tag{14}$$

where here the variables X, Y and Z are given by :

$$\begin{cases} X = f_x(x,y,z) \\ Y = f_y(x,y,z) \\ Z = f_z(x,y,z) \end{cases} \tag{15}$$

The difference with 2D acquisitions lies in the fact that the correction functions X and Y do not depend on function Z any more. The correction can thus be applied in the three directions in any order.

MATERIALS AND METHODS

Most of the current distortion correction methods are based on precomputed displacement tables. These techniques generally involve imaging a phantom of known dimensions, or require knowledge of the mathematical equations of the current in the gradient coils (xviii). The advantage of the phantom-based methods is that the measurements performed take into account the non-linearity of the gradient fields as well as the static variations of the B_0 field. The main disadvantage lies in the limited accuracy due to the discrete aspect of the correction, which often implies an interpolation of several points of the table to compute only one displacement.

Our objective is here to define the expressions of the non-linearities $f_i(x,y,z)$ which connect the real gradients to their theoretical values used during the reconstruction process. The discrete approximation is avoided by using the analytical expressions in the correction functions. These expressions are chosen with respect to the cylindrical geometry of present MR magnets. The field produced along the z axis of the opposed Helmoltz pair is given by (xix) :

$$B_z(z) = \frac{\mu_0 I a^2}{2}\left(\frac{1}{(a^2 + (z - b/2)^2)^{\frac{3}{2}}} - \frac{1}{(a^2 + (z + b/2)^2)^{\frac{3}{2}}} \right) \tag{16}$$

where a is the radius of the coils, b is the distance between the opposed coils and I is the current applied. Using the cylindrical symmetry of the device, the field produced in every point of the space inside the cylinder can be expressed by :

$$B_z(x,y,z) = \sum_{i=0}^{\infty} A_i' (x^2 + y^2)^{2i} \sum_{j=0}^{\infty} B_j' z^{2j+1} \tag{17}$$

where A_i' and B_i' are some constant parameters. The ideal gradient G_z used during the reconstruction process is given by $G_z = A_0' B_0'$. The general expression of $B_z(z)$ is thus :

$$B_z(x,y,z) = G_z z\left(1 + \sum_{i=0}^{\infty} A_i \rho^{2i} \sum_{j=1}^{\infty} B_j z^{2(j-i)}\right) \tag{18}$$

A Golay arrangement is used to encode each of the x an y directions. The field produced in the plane (xOz) in order to encode the direction x is given by :

$$\begin{aligned} B_x(x,z) = {} & \frac{\mu_0 I}{4\pi (x+a)}\left(\frac{b/2 - z}{\sqrt{(b/2 - z)^2 + (x+a)^2}} + \frac{b/2 + z}{\sqrt{(b/2 + z)^2 + (x+a)^2}} \right) \\ & + \frac{\mu_0 I}{4\pi (x-a)}\left(\frac{b/2 - z}{\sqrt{(b/2 - z)^2 + (x-a)^2}} + \frac{b/2 + z}{\sqrt{(b/2 + z)^2 + (x-a)^2}} \right) \end{aligned} \tag{19}$$

The general expression of the field, including the ideal value Gx of the gradient, is developed from the last expression and the symmetry with :

$$B_x(x,y,z) = G_x\, x\,(1 + \sum_{i=0}^{\infty} A_i\, \rho^{2i} \sum_{j=1}^{\infty} B_j\, z^{2(j-i)}) \qquad (20)$$

It can be seen from equations (18) and (20) that for the three sets of coils, the non-linearity functions appear as infinite sums of polynomials in *(x,y,z)* of the general expression :

$$f_\alpha(x,y,z) = \alpha\,(1 + \sum_{i=0}^{\infty} A_i\ (x^2 + y^2)^i \sum_{j=1}^{\infty} B_{ij}\, z^{2(j-i)})\ , \quad \alpha \equiv x, y, z \qquad (21)$$

The variables *x*, *y* and *z* do not represent here the acquisition directions, but set up a static coordinate system whose directions follow the coils axes.

Estimation of the correction functions

A simple cubic phantom was designed in order to estimate the values of the parameters A_i and B_{ij} of the correction functions. Filled with a homogeneous substance (oil), the effects of magnetic susceptibility and chemical shifts simply involve constant voxel shifts along the slice selection and frequency encoding directions. Phantom dimensions were chosen in order to cover a large cerebral volume without exceeding the limits imposed by the receiver (head coil). The edges of the phantom are extracted from the images using an edge detection algorithm that ensures subvoxel precision. The principle, described in figure 1, is to fit the row profile of the gradient image with a gaussian model. Subvoxel accuracy is achieved through the floating point precision of the gaussian means accounting for edges positions.

Detected edges, representing the internal faces of the phantom after an acquisition, are placed in a real coordinate system given by the gradient isocenter and the three acquisition directions. Theoretical internal faces are supplied by the physical dimensions of the phantom. They are analytically described with the equations of two

planes per acquisition direction, defined in the same coordinate system than the detected faces. According to the symmetry of the correction functions, those planes can be computed using detected edges positions and the physical phantom dimensions as shown in figure 2. The resulting cube, entirely characterised by the equations of six planes $x = P_i(y, z)$ defining its surface, represents then the theoretical undistorted image of the phantom. Since the edges of the cube and detected edges in the images are equally affected by the same constant errors due to both chemical shifts and magnetic susceptibility, we assume that the differences in their positions only come from gradient fields non-linearities. Therefore, the operations that transform the set of detected edges into the perfect cube are defined by the three correction functions. The parameters A_i and B_{ij} can be computed in order to minimise the distance between detected edges and their corresponding theoretical positions.

The matching between any detected edge $M(x_d, y_d, z_d)$ and its theoretical position $N(x_c, y_c, z_c)$ in the corresponding face of the cube is achieved through successive approximations of the correction function parameters, using the following algorithm:

- Parameters are initialized with null values. The correction functions at this step are $f_{x0}(x, y, z) = x$, $f_{y0}(x, y, z) = y$ and $f_{z0}(x, y, z) = z$.
- For each slice z of the acquired volume

  For each row y of slice z

  Each detected point $M(x_d, y_d, z_d)$ is matched to a theoretical point $N(x_{c0}, y_{c0}, Z_{c0})$ located in the theoretical plane. Ordinates y_{c0} and z_{c0} are given by $y_{c0} = f_{y0}^{-1}(x_d, y_d, z_d)$ and $z_{c0} = f_{z0}^{-1}(x_d, y_d, z_d)$. Corrected abscissa is then calculated with the plane equation $x_{c0} = P_i(y_{c0}, z_{c0})$.

The minimisation of the distance between points *M* and *N*, according to the general linear least squares criterion (xx), evaluates the parameters of a first correction function f_{x1} such as $x_d = f_{x1}(x_{c0}, y_{c0}, z_{c0})$ and $x_{c0} = f_{x1}^{-1}(x_d, y_d, z_d)$.

This step, repeated twice with two circular permutations, leads to the two other functions f_{y1} such as $y_d = f_{y1}(x_{c0}, y_{c0}, z_{c0})$ / $y_{c0} = f_{y1}^{-1}(x_d, y_d, z_d)$, and f_{z1} such as $z_d = f_{z1}(x_{c0}, y_{c0}, z_{c0})$ / $z_{c0} = f_{z1}^{-1}(x_d, y_d, z_d)$. In this way the correction functions set up, in each step, the theoretical positions that will be used to estimate those functions during the next step. This process is iterated as long as the positions of the theoretical points fluctuate, i.e. is stopped when :

$$\begin{cases} \left| x_{c(n-1)} - x_{cn} \right| < \varepsilon \\ \left| y_{c(n-1)} - y_{cn} \right| < \varepsilon \\ \left| z_{c(n-1)} - z_{cn} \right| < \varepsilon \end{cases} \quad \forall\, x_d, y_d, z_d$$

Finally the application of the functions f_{xn}, f_{yn} and f_{zn} on all the points $M(x_d, y_d, z_d)$ of the initial volume ensures the replacing of these points on their theoretical locations $N(x_c, y_c, z_c)$.

This algorithm was written in C language and was tested on a SUN utltrasparc2 300Mhz workstation under Unix. The time required for post processing is about 2 mn 20 s on a 3D MRI (124x256x256 voxels).

RESULTS

Parameters

Images were acquired on a 1.5T Signa GE scanner (General Electric Medical Systems, Milwaukee, WI) with a generic 3D spoiled GRASS sequence (TR=22 ms, TE=3 ms,

bandwith=16 Khz). A matrix of 256x256 pixels is used for a field-of-view of 256x256 mm^2, and 124 slices of thickness 1.7 mm cover the phantom.

For an optimal correction, the theoretical expression of the correction functions, given by equation (21), indicates that the order of the functions, and so the number of parameters, is supposed to be infinite. However, the limited accuracy of the physical dimensions (± 0.1 mm) and the detected edges positions (± 03 mm) allows a consequent reduction to the number of significant parameters. In practice the functions are developed using an increasing order, starting from one. For each order, the parameters are computed and compared to their corresponding values from the previous developments. This process showed that at the order three, most of the 11 parameters estimated in each direction where not important enough to bring significant changes in the values of the correction functions. So the choice of the order is settled to 2, leading to 5 parameters per acquisition direction. Each function is estimated under the reduced form:

$$f_\alpha(x,y,z) = \alpha\left(1 + K_{\alpha 0}\left(x^2+y^2\right) + K_{\alpha 1}\, z^2 + K_{\alpha 2}\, z^2\left(x^2+y^2\right) + K_{\alpha 3}\left(x^2+y^2\right)^2 + K_{\alpha 4}\, z^4\right) \quad (22)$$

A first set of parameters K_{ij} resulting from the estimation is given in table 1.

The similarity of the parameters K_{xi} and K_{yi} is explained by the identical geometry of the *x* and *y* gradient coils, which differ in theory only by their orientations. Moreover, the order 2 seems to be sufficient to modelize the non-linearities, since the higher order parameters K_{x3}, K_{x4}, K_{y3}, K_{y4} from the two most distorted directions are the less significant. For example, a point located 100 mm from the isocenter is shifted from less than 0.05 mm under the action of those parameters only.

Stability

Several acquisitions of the phantom with different sequences (2D, 3D, Gradient Echo, Spin Echo) and parameters (matrix size, field-of-view, bandwidth and encoding directions) have been used to estimate the correction functions. The results, partially illustrated by figure 3, exhibited no significant differences in the parameters values, showing the stability of the correction functions with the imaging sequences. This also confirms that the voxel shifts induced by the gradient non-linearities only depend on the voxel spatial location. The parameters of the correction can be estimated once and used to correct any further acquisition.

Validation

A basic set of parameters, estimated using the generic 3D SPGR sequence, was used to correct several other acquisitions of the phantom. Corrected edge positions were first compared to their theoretical values, which exhibited a mean difference of less than 0.1% of the voxel size (figure 4). A manufacturer provided correction method (GE 'Grad Warp 2D') was used for the validation. Also based upon the gradient coils geometry, it only acts on the first phase and frequency encoding directions, leaving the slice selection direction uncorrected. A mean difference of 0.5% was found in the right-left and antero-posterior directions between the two correction schemes, and 0.9% in the superior-inferior direction. The first difference is corresponding to a variation of 0.5 mm between the corrections of a point located 100 mm from the center. This small value confirms the equivalence of the two correction schemes and validates the model of the correction functions. However, the more important difference found in the superior-

inferior direction doesn't confirm this equivalence. In order to test the validity of the methods, we used a CT scan of the phantom as another reference for the corrections. The previous edge detection algorithm enabled extraction of both internal and external faces of the phantom from the CT volume. A set of 3D MR acquisitions were performed using two different orientations of the phantom in the head coil. For each acquisition, the reconstructed volume is corrected in post-processing, using Grad Warp and the correction functions. The dimensions of the phantom, extracted from MR images, are compared to the physical dimensions and also to the dimensions extracted from the CT scan. The results are presented in table 2.

As we can see in the first column, the length of the phantom given by Grad Warp after the first acquisition is nearly approaching the theoretical dimension, which is confirmed by the dimension given by the CT scan. The length was oriented in the right-left direction. For the second acquisition, where the length corresponded to the superior-inferior direction, the measurement given by Grad Warp is underestimated by about 2 mm (2 voxels) on a distance of 180 mm. This problem doesn't occur in the function-corrected images, since the parameters are computed in order to register the physical dimensions with the distorted dimensions. The CT scan measurements, compared to the physical and function-corrected dimensions, exhibit no significant variations. These results clearly demonstrates the better performance of the correction functions in the superior-inferior direction.

Experimental results

The first application of the correction scheme was to correct the images of the cubic phantom. Figure 5 shows a sagittal and coronal views of the phantom before and after the correction of a sagittal acquisition. As expected, the initial convex shapes are brought back to their original form in every acquisition directions.

A spherical phantom, filled with a dilution of copper sulfate and from an internal diameter of 100.0 mm was also used for the correction. Figure 6 shows a sagittal and axial views of a sagittal acquisition. We can see a small variation of the edges positions in the right-left direction of the sagittal view. The maximum deviation of 0.7 mm corresponds to a shift of 1.4 pixel. The superior-inferior direction doesn't seem to be affected by gradient non-linearities at such a small distance of the edges from the gradient isocenter. In the other view, both misplaced left-right and antero-posterior edges are corrected from nearly the same shift.

Figure 7 shows an application of the method to the correction of a T1-weighted sagittal acquisition of a healthy volunteer. There is no significant differences between the function-corrected areas (in red) and Grad Warp-corrected areas (green) in the acquisition plane. In the coronal view, distortions from up to 4.2 mm (4 voxels) in the right-left direction are corrected with the functions but unchanged with Grad Warp

DISCUSSION

The analytical expressions of the correction functions, derived from the coils geometry, limit the method to a specific magnet design. The knowledge of the coils geometry implemented on other imaging systems, such as open magnets, is required to define a more suitable set of analytical expression. However, the same method can be used for the correction of images obtained from such scanners.

The loss of quality involved by the numerous interpolations of the voxels can't be avoided when correcting the images. Nevertheless, the correction functions can also be used to correct some topological characteristics of structures without quality loss, instead of correcting the structures themselves.

Geometric distortions correction is clearly required in stereotactic surgery using frame-based registrations, but also in the registration of images obtained with different modalities such as MR-CT for brain anatomy or MR-PET for functional imaging. A method was presented by which one of the most important sources of distortion can be analytically estimated and further corrected in the resultant MR images. The position errors were reduced from several millimeters or voxels down to below the image resolution. Correction functions can be estimated once and applied in post-processing on any acquisition type without changing the acquisition time. It can be used as a full 3D correction in replacement to the actual 2D corrections implemented on most MR scanners

ACKNOWLEDGMENTS

This study was carried out within the framework of the 'Pôle Traitement et Analyse d'Images de Caen'. The research was funded in part by the General Electric Medical Systems society and the 'Fond Social Européen'.

APPENDIX

Effect of the non-linearities on the slice profile and slice position in 2D imagery

The effect of a gradient field $G_z(z) = z\,G_p$ applied in the z direction is to select tissues with specific precession frequencies, given by the Larmor frequency of the spin system $\omega_z(z) = \omega_0 + \gamma\, z\, G_p$.

A selective RF pulse centered on ω_α with a length $\delta\omega$, applied while $G_z(z)$ is turned on, activates the magnetization only within the slice z of thickness δz given by

$$\begin{cases} z = \dfrac{\omega_\alpha}{\gamma\, G_p} \\ \delta z = \dfrac{\delta\omega}{\gamma\, G_p} \end{cases}$$

The theoretical signal generated at the point (x,y) is then:

$$M_t(x,y,z) = \int_{z}^{z+\delta z} M(x,y,z')\,dz' \tag{23}$$

By introducing the non-linearities $f_z(x,y,z)$ into the expression of the slice encoding gradient, which becomes $G_z(x,y,z) = f_z(x,y,z)\,G_p$, the real precession frequency becomes $\omega_{rz}(z) = \omega_0 + \gamma\, f_z(x,y,z)\,G_p$.

The actual magnetization excited by the selective RF pulse is:

$$M_r(x,y,z) = \int_{f_z^{-1}(x,y,z)}^{f_z^{-1}(x,y,z+\delta z)} M(x,y,z')\,dz' \tag{24}$$

Equations (18) and (19) show that the theoretical slice $(z, \delta z)$ is shifted to the real set $(z', \delta z')$ (Figure 1) fixed by:

$$\begin{cases} z' = f_z^{-1}(x,y,z) \\ \delta z' = \left| f_z^{-1}(x,y,z+\delta z) - f_z^{-1}(x,y,z) \right| \end{cases}$$

Equation (24) can be rewritten as:

$$M_r(x,y,z) = \int_z^{z+\delta z} M\left(x,y,f_z^{-1}(x,y,z')\right)\frac{\partial f_z^{-1}(x,y,z')}{\partial z'}dz' \tag{25}$$

and, with slight variations of $\frac{\partial f_z^{-1}(x,y,z')}{\partial z'}$ in the slice thickness, as:

$$\begin{aligned} M_r(x,y,z) &\approx \frac{\partial f_z^{-1}(x,y,z)}{\partial z}\int_z^{z+\delta z} M\left(x,y,f_z^{-1}(x,y,z')\right)dz' \\ &= \frac{\partial f_z^{-1}(x,y,z)}{\partial z} M_t\left(x,y,f_z^{-1}(x,y,z)\right) \end{aligned} \tag{26}$$

The theoretical magnetisation is thus

$$M_t(x,y,z) = \frac{\partial f_z(x,y,z)}{\partial z} M_r\left(x,y,f_z(x,y,z)\right) \tag{27}$$

Two dimensions

Due to *T2* decay and the application of two encoding gradients $G_l(t)$ and $G_c(t)$, the theoretical signal emitted at time *t* and repetition *k* after the slice selection process is in every point of the space:

$$s(x,y,z,t,k) = M_r(x,y,z)\, e^{-\frac{t+TE}{T2(x,y,z)}} e^{j\gamma\left[\int_0^t x\,G_l(t')\,dt' + \int_0^{\tau_y} k\,y\,G_c(t')\,dt'\right]} \tag{28}$$

With both $G_l(t)$ and $G_c(t)$ independent of time during signal acquisition, Eq.(28) becomes

$$s(x,y,z,t,k) = M_r(x,y,z)\, e^{-\frac{t+TE}{T2(x,y,z)}}\, e^{j\gamma\left[x\,G_l\,t + y\,k\,G_c\,\tau_y\right]} \tag{29}$$

The non-linearities are introduced here by replacing in the signal expression $x\ G_l$ with $G_{rx}(x,y,z) = f_x(x,y,z)\ G_l$ and $y\ G_c$ with $G_{ry}(x,y,z) = f_y(x,y,z)\ G_c$. The acquired signal from the selected slice *z* is :

$$
\begin{aligned}
S_r(z,t,k) &= \int_{FOVx}\int_{FOVy} s(x,y,z,t,k)\,dy\,dx \\
&= \int_{FOVx}\int_{FOVy} M_r(x,y,z)\, e^{-\frac{t+TE}{T2(x,y,z)}} e^{j\gamma f_y(x,y,z)kG_c\tau_y}\; e^{j\gamma f_x(x,y,z)G_l t}\,dy\,dx
\end{aligned}
\tag{30}
$$

A first Fourier transform of $S_r(z,t,k)$ gives:

$$
\begin{aligned}
I_y(y,z,t) &= \frac{1}{FOV_y}\sum_{k=-Ny/2}^{Ny/2} S(z,t,k)\, e^{-j\gamma y k G_c \tau_y} \\
&= \frac{1}{FOV_y}\sum_{k=-Ny/2}^{Ny/2}\left[\int_{FOVx}\int_{FOVy} M_r(x,y',z)\, e^{-\frac{t+TE}{T2(x,y',z)}}\; e^{j\gamma f_y(x,y',z)kG_c\tau_y}\right. \\
&\qquad \left.\times\; e^{j\gamma f_x(x,y',z)G_l t}\,dy'\,dx\right] e^{-j\gamma y k G_c\tau_y} \\
&= \int_{FOVx}\int_{FOVy} M_r(x,y',z)\, e^{-\frac{t+TE}{T2(x,y',z)}}\; e^{j\gamma f_x(x,y',z)G_l t}\; H_y(y - f_y(x,y',z))\,dy'\,dx
\end{aligned}
\tag{31}
$$

A second Fourier transform gives with $\Delta t = t\,Fe$:

$$
\begin{aligned}
I_a(x,y,z) &= \frac{1}{FOV_x}\sum_{t=-Nx/2}^{Nx/2} I_y(y,z,t)\, e^{-j\gamma x G_l \Delta t} \\
&= \frac{1}{FOV_x}\sum_{t=-Nx/2}^{Nx/2}\left[\int_{FOVx}\int_{FOVy} M_r(x',y',z)\, H_y(y - f_y(x',y',z))\, e^{-\frac{\Delta t+TE}{T2(x',y',z)}}\right. \\
&\qquad \left.\times\; e^{j\gamma f_x(x',y',z)G_l t}\,dy'\,dx'\right] e^{-j\gamma x G_l \Delta t} \\
&\approx \int_{FOVx}\int_{FOVy} M_r(x',y',z)\, e^{-\frac{TE}{T2(x',y',z)}}\, H_y(y - f_y(x',y',z))\, H_x(x - f_x(x',y',z))\,dy'\,dx'
\end{aligned}
\tag{32}
$$

The T2 decay during the readout is neglected here for more simplicity. The last expression of the intensity, shifted in both x and y directions, can be seen as the received magnetisation convolved with the Fourier transforms H of the gradients :

$$
I_a(f_x(x,y,z), f_y(x,y,z), z) = M_r(x,y,z) e^{-\frac{TE}{T2(x,y,z)}} \otimes H_x(f_x(x,y,z)) \otimes H_y(f_y(x,y,z))
\tag{33}
$$

The expression of an undistorted image is obtained from Eq. (33) where $f_x(x,y,z) = x$ and $f_y(x,y,z) = y$:

$$I_c(x,y,z) = M_t(x,y,z)e^{-\frac{TE}{T2(x,y,z)}} \otimes H_x(x) \otimes H_y(y) \tag{34}$$

with the system of variables *X*, *Y*, *Z* given by

$$\begin{cases} X = f_x(x, y, Z) \\ Y = f_y(x, y, Z) \\ Z = f_z(x, y, z) \end{cases}$$

the correction of the slice profile, given by equation (27), brings to the relation between I_c and I_a :

$$I_c(x,y,z) = I_a(X,Y,Z)\frac{\partial Z}{\partial z} \otimes H_x(X) \otimes H_y(Y) \tag{35}$$

Three dimensions

Voxels are discriminated in 3D imagery by a constant readout gradient $x.G_l$ and two phase encoding gradients $y\ k\ G_c$ and $z\ p\ G_p$. The received signal under the action of the various gradients is expressed by:

$$s(x,y,z,t,k) = M_r(x,y,z)e^{-\frac{t+TE}{T2(x,y,z)}}\ e^{j\gamma\left[x G_l t + y k G_c \tau_y + z p G_p \tau_z\right]} \tag{36}$$

The introduction of the non-linearities in the expressions of the gradients, that become $G_x(x,y,z) = f_x(x,y,z)\ G_l$, $G_y(x,y,z) = f_y(x,y,z)\ G_c$ and $G_z(x,y,z) = f_z(x,y,z)\ G_p$, yields in the sampled signal:

$$\begin{aligned} S_r(z,t,k) = & \int_{FOVx}\int_{FOVy}\int_{FOV_z} M_r(x,y,z)e^{-\frac{t+TE}{T2(x,y,z)}} \\ & \times e^{j\gamma\left[f_z(x,y,z)\,p G_p \tau_z + f_y(x,y,z)\,k G_c \tau_y + f_x(x,y,z)\,G_l t\right]} dz\,dy\,dx \end{aligned} \tag{37}$$

Three successive Fourier transforms, and the same straightforward algebric calculation than in 2D, bring to the relationship between corrected and acquired image:

$$I_c(x,y,z) = I_a(X,Y,Z)\frac{\partial X}{\partial x}\frac{\partial Y}{\partial y}\frac{\partial Z}{\partial z} \tag{38}$$

where here

$$\begin{cases} X = f_x(x,y,z) \\ Y = f_y(x,y,z) \\ Z = f_z(x,y,z) \end{cases}$$

REFERENCES

Figure 1

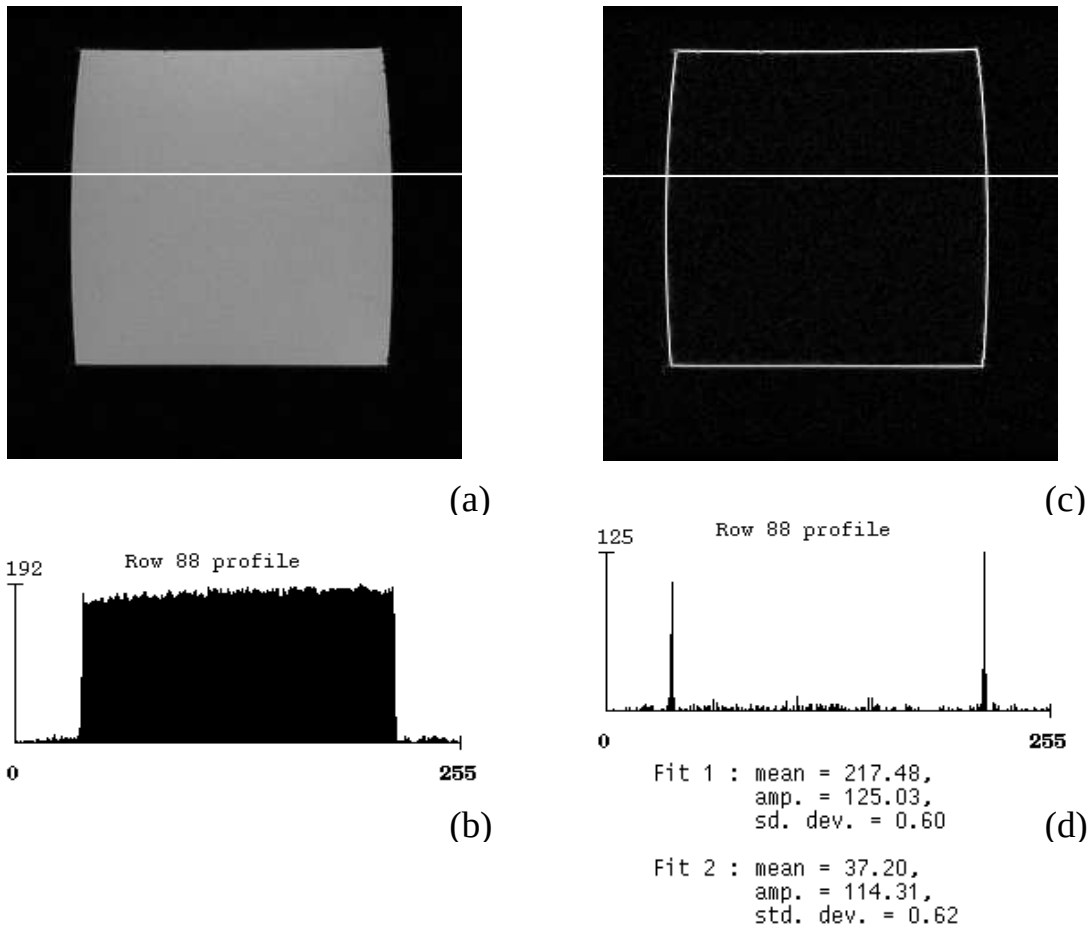

Figure 1. Edge localisation principle.

Each image of the volume is computed (a). The profile of each line is extracted from the images (b). A one dimensional derivative of the profile enables to extract the peaks

representing the edge positions (c). A gaussian fit on each significant peak gives an accurate estimation of the edge positions (d).

Figure 2

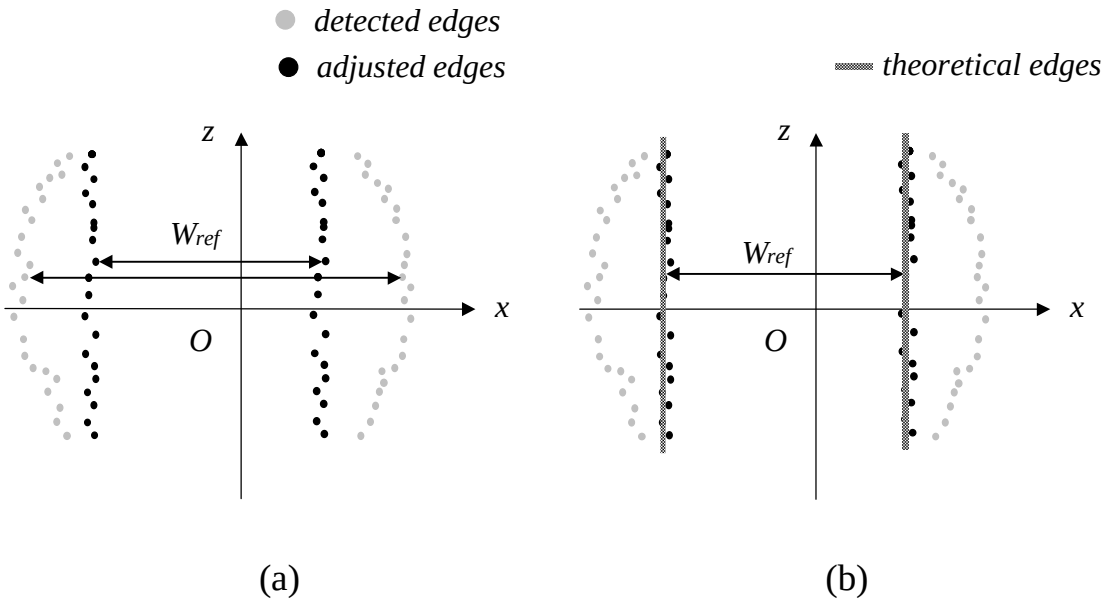

Figure 2. Registration of the imaged and physical phantom.

Detected edges are adjusted line by line such as their distances fit the physical width W_{ref} of the phantom (a). Theoretical planes $x_i=A_i y+B_i z+C_i$ are computed using the least squares criterion on adjusted edges of all slices (b).

Figure 3

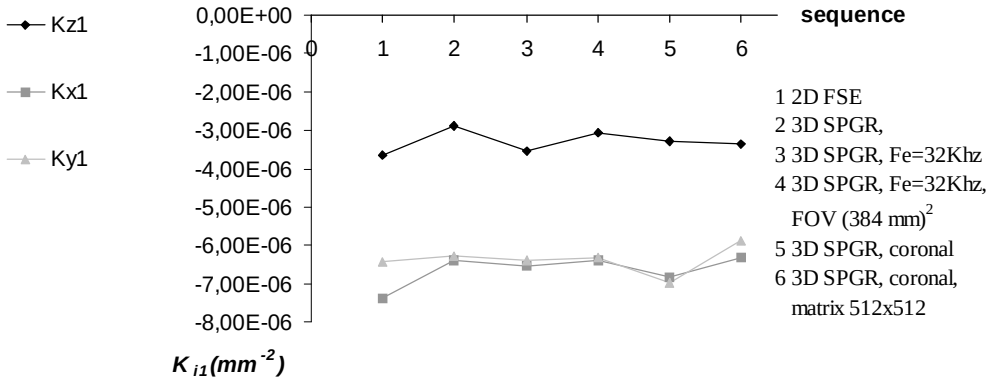

Figure 3. K_{x1}, K_{y1} and K_{z1} variations with the acquisition sequences. Generic parameters are: matrix=256x256 pixels, field-of-view=256x256 mm^2, 124 slices of thickness 1.7 mm in the sagittal plane (yOz), bandwith=16 Khz.

Figure 4

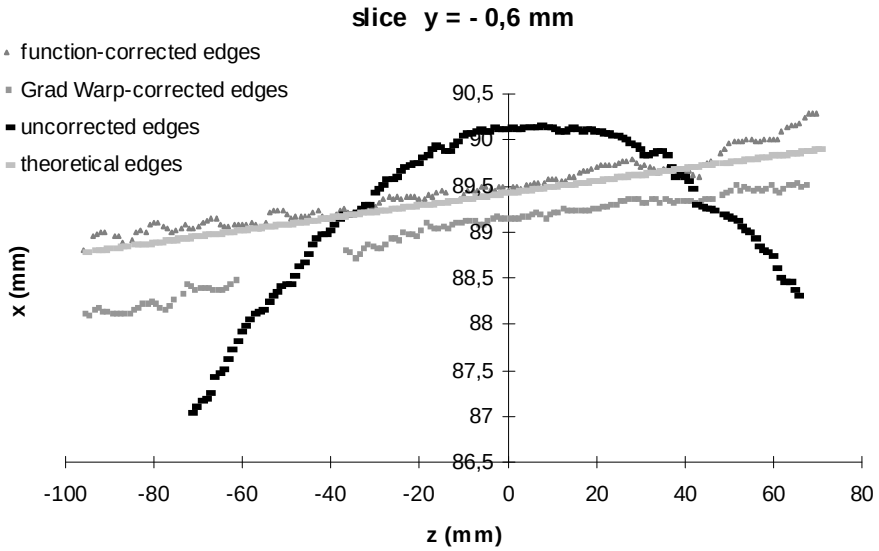

Figure 4. Right edges of a coronal slice of the phantom.

Images are acquired with a 3D SPGR sequence. At 0.6 mm far from the gradient isocenter, uncorrected abscissae go up to 2.6 mm from their theoretical positions

Figure 5

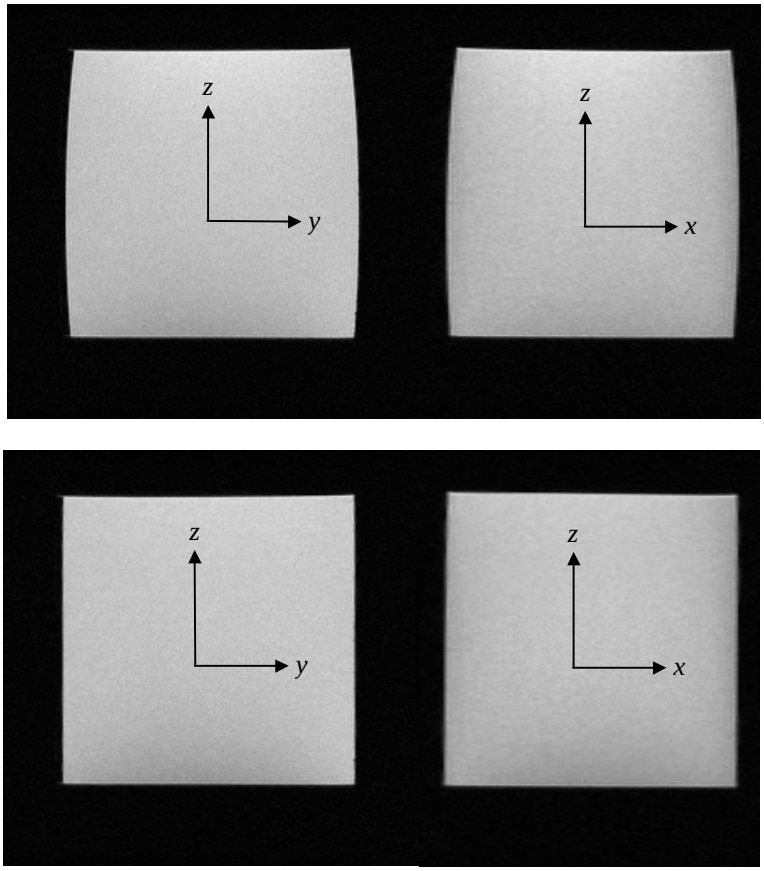

Figure 5. Correction of the cubic phantom.

The top left (sagittal) and top right (coronal) images are constructed from an acquisition without any gradient correction. The bottom images represent the same slices after the correction with the functions.

[i] Haacke E.M., Tkach J.A. Fast MR Imaging: Techniques and Clinical Applications. AJR 1990; 155:951-964.

[ii] Korach G., Minier T., Vignaud J. Manuel de techniques de l'Imagerie par Résonance Magnétique, Editions Nasson, Paris 1992

[iii] Schad L., Lott S., Schmitt F., Sturm V., Lorenz W.J. Correction of Spatial Distortion in MR Imaging : A Prerequisite for Accurate Stereotaxiy. Journal of Computer Assisted Tomography 1987; 11(3):499-505.

[iv] Wells W.M., Grimson W.E.L., Kikinis R., Jolesz J.A. Adaptative Segmentation of MRI Data. IEEE Transactions on Medical Imaging 1996; 15(4):429-442.

[v] Bandetinni P.A., Wong E.C. Effect of Biophysical and Physiologic Parameters on Brain Activation-Induced R_2^* and R_2 changes : Simulations using a deterministic Diffusion Model. International Journal of Imaging Systems and Technology 1995; 6 :133-152.

[vi] Michiels J., Bosmans H., Pelgrims P., Vandermeulen D., Gybels J., Marchal G., Suetens P. On the Problem of Geometric Distortion in Magnetic Resonance Images for Stereotactic Neurosurgery. Magnetic Resonance Imaging 1994; 12(5):749-765.

[vii] Walton L., Hampshire A., Forster D.M.C., Kemeny A.A. A phantom study to assess the accuracy of stereotactic localization, using T1 weighted magnetic resonance imaging with the Leskell stereotactic system. Neurosurgery 1996; 38(1):170-178.

[viii] Sumanaweera T.S., Glover G., Song S., Adler J., Napel S. Quantifying MRI geometric distortion in tissue. Magnetic Resonance in Medicine 1994; 31:40-47.

[ix] Moerland M.A., Beersma R., Bhagwandien R., Wijrdeman H.K., Bakker C.J.G. Analysis and Correction of Geometric Distortions in 1.5T Magnetic Resonance

Images for use in Radiotherapy Treatment Planning. Physics in Medicine and Biology 1995; 40:1651-1664.

[x] Sun L., Aletras A.H., Schmalbrock P., Skinner T.E., Chakeres D., Irsik R., Robitaille P-M.L. Water and Fat MR Imaging with Chemical Shift Selective 3D Steady State Methods. Magnetic Resonance in Medicine 1994; 31:359-364.

[xi] Schenck J.F. The role of magnetic susceptibility in magnetic resonance imaging : MRI magnetic compatibility of the first and second kinds. Medical Physics 1996; 23(6):815-850.

[xii] Posse S. Direct Imaging of Magnetic Field Gradients by Group Spin-Echo selection. Magnetic Resonance in Medicine 1992; 25:12-29.

[xiii] Maurer C.R., Aboutanos G.B., Dawant B.M., Gadamsetty S., Margolin R.A., Maciunas R.J., Fitzpatrick J.M. Effect of Geometrical Distortion Correction in MR on Image Registration Accuracy. Journal of Computer Assisted Tomography 1996; 20(4):666-679.

[xiv] Zhu X.X., Macdonald P.M. Empirical compensation function for eddy current effects in pulsed field gradient nuclear magnetic resonance experiments. Solid State Magnetic Resonance 1995; 4:217-227.

[xv] Hughes D.G., Robertson S., Allen P.S. Intensity Artifacts in MRI Caused by Gradient Switching in an Animal-Size NMR Magnet. Magnetic Resonance in Medicine 1992; 25:167-179.

[xvi] Hinshaw, Lent A.H. An Introduction to NMR Imaging: From the Bloch Equation to the Imaging Equation. Proceedings of the IEEE 1983; 71(3):338-350.

[xvii] Introduction à l'IRM, Guinet, J. Grellet, Editions Masson, Paris (1992)

[xviii] Sumanaweera T.S., Adler J.R., Napel S., Glover G.H. Characterization of Spatial Distortion in Magnetic Resonance Imaging and Its Implications for Stereotactic Surgery. Neurosurgery 1994; 35(4):1-9.

[xix] E. Durand, Electromagnetisme Tome I, Editions Masson, Paris (1966)

[xx] Press W.H., Teukolsky S.A., Vetterling W.T., Flannery B.P. Numerical recipes in C: The Art of Scientific Computing. Cambridge University Press 1992.